South African Journal of Chemical Engineering 34 (2020) 31–46

Contents lists available at ScienceDirect

South African Journal of Chemical Engineering

journal homepage: www.elsevier.com/locate/sajce

Modelling the Dynamics of Granular Particle Interactions in a Vortex Reactor using a Coupled DPM-KTGF Model

B. Oyegbile[a,*], G. Akdogan[a], M. Karimi[b]

[a] Department of Process Engineering, Stellenbosch University, Banghoek Road, Stellenbosch 7600 South Africa
[b] Department of Chemistry and Chemical Engineering, Chalmers University of Technology, SE-41296 Gothenburg, Sweden

ARTICLE INFO

Keywords:
Hydrodynamics
Turbulence
Restitution coefficients
KTGF
DPM

ABSTRACT

In this work, a shear-driven two-phase particulate flow of monodispersed and polydispersed granular materials has been studied experimentally and numerically as a function of solids concentration and restitution coefficients for different operating speeds *N* (70 -130 *rpm*) in a lab-scale rotor-stator agglomeration reactor. A coupled computational fluid-particle dynamics (CFPD) model was developed consisting of a steady-state flow field of the continuous phase coupled to a transient particle tracking of the discrete phase. This was achieved via a one-way coupling between the continuous and the discrete phase by including the effect of drag, lift, pressure gradient, virtual mass forces, as well as granular collisional forces in describing the particle-particle, particle-wall and the fluid-particle interactions. The spatiotemporal evolution of the flow pattern, discrete phase properties, and influence of the operating conditions on the granular properties were characterized. The validation of the numerical model developed in this study was carried out based on the theoretical analysis of the rotor-stator flow and the PIV flow measurements. The results showed that the particle sizes were uniformly distributed within the reactor after steady-state conditions, while a small region of high particle concentration was observed near the rotor due to low vorticity and turbulent intensity around the region. In terms of the operating conditions, the restitution coefficients and the operating speeds do not have a significant influence on the granular properties apart from the small region around the shaft where there is a correlation between these parameters. The particle sizes, however, show a positive correlation with the granular properties. Also, a wider particle size distribution was observed axially towards the stator, which might be attributed to the pumping effect of the Batchelor flow in this direction. It was also concluded that the discrete phase velocity does not seem to vary significantly with the restitution coefficients. Furthermore, the vertical velocity and vorticity profiles give a reasonably good agreement between the CFPD model predictions and PIV measurements. The minor observed deviations were mainly due to some of the experimental limitations rather than the robustness of the CFPD model or the numerical code.

1. Introduction

Efficient fluid-particle mixing and dispersion is highly indispensable in many industrial, pharmaceutical, biological, and environmental processes involving fluid-particle interactions. Mixing, transport, aggregation and deposition of particulate solids occur simultaneously in many natural, biological and engineered processes (Chaumeil and Crapper, 2014; Greifzu et al., 2016; Haghnegahdar et al., 2018; Njobuenwu and Fairweather, 2018; Yu et al., 2016). Therefore, in studying the dynamics of these systems, the spatial and temporal evolution of the properties of discrete phase dispersed within the continuous phase is of great interest. In solid-liquid mixing especially in agitated vessels, there exists three distinct phases of particle dispersion within the fluid phase namely: on-bottom, off-bottom, and fully suspended phases (Derksen, 2003). The mixing efficiency in any fluid-particle system largely depends on the dispersion uniformity in terms of the spatial and temporal distribution and homogeneity of the discrete phase within the continuous phase. This mixing efficiency can be assessed in terms of specie attributes such as suspended speed, coefficient of variation, solids mass concentration, volume fraction, number density and size distribution within the mixing vessel (Wadnerka et al., 2012).

Computational Fluid Dynamics (CFD) offers a flexible and robust platform for the investigation of fluid-particle interactions in simple to complex reactor systems, and multitude of flow scenarios occurring in a variety of process conditions (Tu et al., 2018). The application of CFD to model particulate flow problems has been growing in popularity over the past decade. Several modelling techniques have been proposed with

* Corresponding author.
E-mail address: oyegbile@sun.ac.za (B. Oyegbile).

https://doi.org/10.1016/j.sajce.2020.05.008
Received 9 March 2020; Received in revised form 4 May 2020; Accepted 19 May 2020

Nomenclature

List of Symbols

C_D	Drag coefficient
C_L	Lift coefficient
d_p	Particle diameter (m)
Re_p	Particle relative Reynolds number
Re_ω	Particle rotational Reynolds number
e_{ss}	Normal coefficient of restitution
p	Pressure (Pa)
p_s	Solids pressure
t	Time (s)
g	Gravitational acceleration (ms^{-2})
$g_{0,ss}$	Radial distribution function
v	Velocity (ms^{-1})

Greek symbols

β	Drag coefficient between continuous and dispersed phase
$\overset{\gamma}{s}$	Dissipation rate of the turbulent kinetic energy
α_s	Solids volume fraction
θ	Granular temperature ($m^{-2}s^{-2}$)
λ_s	Solids bulk viscosity ($kgm^{-1}s^{-1}$)
μ_s	Solids shear viscosity ($kgm^{-1}s^{-1}$)
μ	Dynamic viscosity ($kgm^{-1}s^{-1}$)
ρ	Density of liquid phase (kgm^{-3})
ρ_s	Density of solid phase (kgm^{-3})
μ_m	Molecular viscosity ($kgm^{-1}s^{-1}$)
μ_t	Turbulent viscosity ($kgm^{-1}s^{-1}$)
φ_{ls}	Interphase kinetic energy transfer
ω_p	Particle angular velocity (s^{-1})
Ω	Relative fluid-particle angular velocity (s^{-1})

Subscripts

int	Interaction
col	collisional
fr	Friction
kin	Kinetic
max	Maximum

some encouraging results both in terms of the model predictions and computational efficiency. The Eulerian-Eulerian and Eulerian-Lagrangian models such as the two fluid model (TFM), discrete phase model (DPM), discrete element method (DEM), kinetic theory of granular flow (KTGF), frictional stress model (FSM) etc., are a few of the widely-used modelling approaches in the scientific community especially in the modelling of particle-laden flows (Norouzi et al., 2016; Tu et al., 2018).

In the numerical simulation of the hydrodynamics of the discrete phase dispersed within a continuous phase, an accurate resolution of the fluid-particle, particle-particle and particle-wall interaction forces is highly indispensable to obtain an accurate result. The ability to predict the dynamics of the dispersed phase (i.e. dispersion, transport, coalescence/agglomeration, breakage, deposition etc.) depends on an accurate resolution of all the forces experienced by individual particles within a turbulent flow field. However, it is worth pointing out that quantifying all the forces that mediate fluid-particle interactions is a daunting task (Bellani and Variano, 2012). The particle-particle and particle-wall interaction forces can be implicitly resolved using the kinetic theory of granular flow (KTGF) or explicitly resolved using the discrete element method (DEM). This is then coupled to the fluid flow via mass, momentum and energy exchange between the continuous and the dispersed phase to account for the fluid-particle interactions. Coupled CFD-DEM is widely used for the simulation of many flow problems involving fluid-particle interactions due to its high degree of accuracy in resolving nearly all the fluid-particle and particle-particle interaction forces (Chaumeil and Crapper, 2014; Chu and Yu, 2008; Fanelli et al., 2006; Hellesto et al., 2016; Vångö et al., 2018; Zhu et al., 2007).

In spite of its accuracy, one main drawback of the DEM approach is the huge computational demand even for simple multiphase flows with low to moderate solids concentration which limits the scope of its application (Cloete et al., 2012; Schellander, 2014). Over the past decade, there has been a steady improvement in computing power and coupled CFD-DEM is increasingly being used to simulate flows with hundreds of thousands to millions of particles by using efficient numerical algorithms and parallelization (Norouzi et al., 2016). However, in most of the practical industrial flows, the number of particles can range from several millions to billions which significantly increases the simulation time thereby limiting the scope of applications of DEM on industrial scale (Cloete et al., 2012; Xie and Luo, 2018). Coupled DPM-KTGF approach on the other hand offers a more reasonable compromise in terms of the computational demand and numerical accuracy, and therefore more computationally efficient (Darelius et al., 2008; Hashemisohi et al., 2019). Several authors have also argued that highly coupled simulations like the DEM are sometimes unnecessary especially for dilute flows with binary collisions, as reasonable abstractions can be made while still capturing the essential features of the flow (Furtney et al., 2013; Michaelides et al., 2016; Norouzi et al., 2016). The KTGF model describes an interaction force $F_{interaction}$ for a particulate flow based on the particulate phase solids stress tensor $\overline{\overline{\tau}}_s$ using the kinetic theory of granular flow. The model which is analogous to the kinetic theory of gas that describes the thermal motion of molecules in a dense gas, is used to derive the solids pressure and solids stresses arising from the random motion of the discrete particles taking into account the inelastic nature of the granular phase. This coupled model also takes into account the fact that when particles collide, energy is dissipated in the form of deformation and heat by using coefficients of elastic restitution to characterize the loss of momentum during collisions. This approach which is ideally suitable for dilute flows, may be extended to prolonged and friction-dominated particle-particle interactions in dense flows by using the frictional stress (FSM) and dense discrete phase model (DDPM). The idealized particle-particle interaction forces are not explicitly resolved as in the soft sphere or classical DEM approach but are modelled, thereby resulting in a much faster computational turnaround especially for simple fluid-particle interactions (Norouzi et al., 2016). Several authors have also successfully employed this alternative modelling approach to reduce the computational demand by applying KTGF approach to model the particle-particle interactions based on the continuum approach within the Eulerian framework (Darelius et al., 2008; Passalacqua and Marmo, 2009; Taghizadeh et al., 2018; Wadnerkar et al., 2016).

A quick survey of the literature reveals a large body of scientific work on the applications of DEM as compared to the coupled DPM-KTGF approach. Cloete et al. applied different fluid-particle models to study dilute gas-solid flow using two modelling approaches namely: Eulerian-Eulerian two-fluid model (TFM-KTGF) and Eulerian-Lagrangian (DDPM-KTGF) model. These models were validated against each other and the results show a close agreement between the two models, with the observed minor differences in the results attributed to the formation of delta shocks which was better captured by DDPM-KTGF approach (Cloete et al., 2012). In a similar study by Gannt and Gatzke, coupled CFD-DEM and DPM-KTGF models were simultaneously applied to the simulation of particulate flow in a high-shear mixer (Gannt and Gatzke, 2006). The results from their work shows a good

agreement between the two fluid-particle models under idealized conditions, while variations were observed as the process conditions become less ideal. The observed deviation might be attributed to some of the assumptions regarding particle sphericity, rigidity and smoothness in the KTGF model in resolving the particle-particle interactions (Xie and Luo, 2018). In addition to incorporating the Brownian and shear forces into the KTGF model, Weber and Hrenya (Weber and Hrenya, 2006) in their study extended the scope of KTGF approach to include non-contact cohesive interparticle forces such as the van der Waals forces using the square well model. The approach presented in their study opened up the possibility of using the coupled KTGF model to account for particle-particle collisions, coalescence and aggregation due to non-contact forces.

The aim of this CFD study is to carry out a qualitative and quantitative hydrodynamic analysis of the granular particle interactions in a rotor-stator particle agglomeration reactor using the Eulerian-Lagrangian one-way coupling. Owing to the complexity of the agglomeration process, modelling effort is devoted to the investigation of the particle-particle and particle-wall interactions in the reactor. The numerical simulation was performed by coupling the discrete phase model (DPM) with the KTGF model to study the spatiotemporal properties of the dilute particulate flow as well as the particle trajectory using ballotini and sand as model particles. The model was subsequently used to study the influence of the operating conditions such as the restitution coefficients, operating speed as well as the particle dispersity on the flow characteristics. The modelling results were verified using the Particle Image Velocimetry (PIV) experimental data from the single-phase flow analysis. This CFPD model can also be extended to dense particulate flows by extending the capability of both the KTGF and DPM models using the frictional stress model (FSM) in combination with Dense Discrete Particle Model (DDPM) in order to account for the increased particle-particle contacts and frictional effects.

2. CFPD Model Development

2.1. Continuous Phase Conservation Equations

The dispersion of particles in a shear flow is modelled using a Eulerian-Lagrangian framework with the particle-particle interaction force $F_{interaction}$ accounted for using the kinetic theory of granular flow. The Reynolds averaged (RANS) conservation equations of mass and momentum for an incompressible flow can be written as follows Eqs. 1-(2) ("ANSYS Fluent Theory Guide 18.2," 2017; Oyegbile and Akdogan, 2018):

$$\frac{\partial \rho}{\partial t} + \nabla\cdot(\rho\vec{v}) = \quad S_{c,d_p} \tag{1}$$

$$\frac{\partial}{\partial t}(\rho\vec{v}) + \nabla\cdot(\rho\vec{v}\vec{v}) = \ -\nabla\vec{p} + \nabla\cdot\mu_{eff}[\nabla\vec{v} + (\nabla\vec{v})^T] + \rho\vec{g} + \vec{S}_{m,\,d_p} \tag{2}$$

where, ρ is the density, p is the static pressure, $\vec{v}$ is the velocity vector, S_{c,d_p} is the source term that represent the mass added to the continuous phase by the dispersed phase or any user-defined mass source and this is zero by default, $\rho\vec{g}$ is the gravitational force, $\vec{S}_{m,\,d_p}$ is a source term representing the interphase exchange of momentum arising from particle-particle and fluid-particle interactions. The effective viscosity μ_{eff} and the momentum transfer between the discrete and the continuous phase are given in Eqs. 3 and 4 ("ANSYS Fluent Theory Guide 18.2," 2017).

$$\mu_{eff} = \mu_m + \mu_t = \mu_m + \rho C_\mu \frac{k^2}{\varepsilon} \tag{3}$$

$$\vec{S}_{m,\,d_p} = \ \sum\left(\frac{18\mu C_D R_e}{\rho_p {d_p}^2 24}(u_p - u) + F_{other}\right)\dot{m}_p\Delta t \tag{4}$$

Table 1
Summary of DPM and KTGF model parameters for the numerical simulation

Simulation parameters	Model equations
Drag Force	$\vec{F_D} = \frac{18\mu C_D Re_p}{24\rho_p {d_p}^2}$ ("ANSYS Fluent Theory Guide 18.2," 2017; Cloete et al., 2012)
Spherical drag coefficient	$C_D = a_1 + \frac{a_2}{Re_p} + \frac{a_3}{{Re_p}^2}$ ("ANSYS Fluent Theory Guide 18.2," 2017)
Particle relative Reynolds number	$Re_p = \frac{\rho d_p \lvert\overline{u_p} - \bar{u}\rvert}{u}$ ("ANSYS Fluent Theory Guide 18.2," 2017; Darelius et al., 2008)
Rotational Drag Toque	$\vec{M} = C_\omega \frac{\rho}{2}\bar{\Omega}\bar{\Omega}{r_p}^5$ (Lukerchenko et al., 2012)
Rotational drag coefficient	$C_\omega = \frac{6.45}{\sqrt{Re_\omega}} + \frac{32.1}{Re_\omega}$ ("ANSYS Fluent Theory Guide 18.2," 2017)
Particle rotational Reynolds number	$Re_\omega = \frac{\rho_f\lvert\vec{\Omega}\rvert{d_p}^2}{4\mu_f}$ ("ANSYS Fluent Theory Guide 18.2," 2017)
Turbulent drag modification factor	$\eta = 1 + K((\frac{d}{\lambda})^3)$ ("ANSYS Fluent Theory Guide 18.2," 2017; Wadnerka et al., 2012)
Saffman lift force	$\vec{F_L} = \frac{2K\nu^{\frac{1}{2}}\rho d_{ij}}{\rho_p d_p (d_{lk}d_{kl})^{\frac{1}{4}}}(\vec{u} - \vec{u_p})$ ("ANSYS Fluent Theory Guide 18.2," 2017)
Magnus rotational lift force	$\vec{F_{RL}} = \frac{1}{2}A_p C_{RL}\rho_f \frac{\lvert\vec{V}\rvert}{\vec{\Omega}}$ ("ANSYS Fluent Theory Guide 18.2," 2017)
Rotational lift coefficient	$C_{RL} = 0.45 + (\frac{Re_\omega}{Re_p} - 0.45)exp(-0.05684{Re_\omega}^{0.4}{Re_p}^{0.3})$ ("ANSYS Fluent Theory Guide 18.2," 2017)
Virtual mass force	$\vec{F} = C_{vm}\frac{\rho}{\rho_p}(\vec{u_p}\vec{\nabla u} - \frac{d\vec{u_p}}{dt})$ ("ANSYS Fluent Theory Guide 18.2," 2017)
Pressure gradient force	$\vec{F} = \frac{\rho}{\rho_p}\vec{u_p}\nabla\vec{u}$ ("ANSYS Fluent Theory Guide 18.2," 2017)
Solids stress tensor	$\bar{\bar{\tau}}_s = -p_s\bar{I} + \alpha_s\mu_s(\nabla\overline{v_s} + (\nabla\overline{v_s})^T) + \alpha_s(\lambda_s - \frac{2}{3}\mu_s)\nabla\cdot\overline{v_s}\bar{I}$ ("ANSYS Fluent Theory Guide 18.2," 2017)
Solids pressure	$p_s = \alpha_s\rho_s\Theta_s + 2\rho_s(1 + e_{ss})\alpha_s{}^2 g_{0,ss}\Theta_s$ ("ANSYS Fluent Theory Guide 18.2," 2017)
Solids shear viscosity	$\mu_s = \mu_{s,col} + \mu_{s,kin}$ ("ANSYS Fluent Theory Guide 18.2," 2017)
Solids bulk viscosity	$\lambda_s = \frac{4}{3}\alpha_s{}^2\rho_s d_s g_{0,ss}(1 + e_{ss})(\frac{\Theta_s}{\pi})^{\frac{1}{2}}$("ANSYS Fluent Theory Guide 18.2," 2017)
Granular temperature	$\Theta_s = \frac{1}{3}(u_{s,i}u_{s,i})$ ("ANSYS Fluent Theory Guide 18.2," 2017)
Collisional energy dissipation rate	$\gamma_{\Theta s} = 3(1 - {e_{ss}}^2)\varepsilon_s{}^2\rho_s g_{0,ss}\Theta_s(\frac{4}{d_p}\sqrt{\frac{\Theta_s}{\pi}} - \nabla\vec{v_s})$ (Cloete et al., 2012; Taghizadeh et al., 2018)

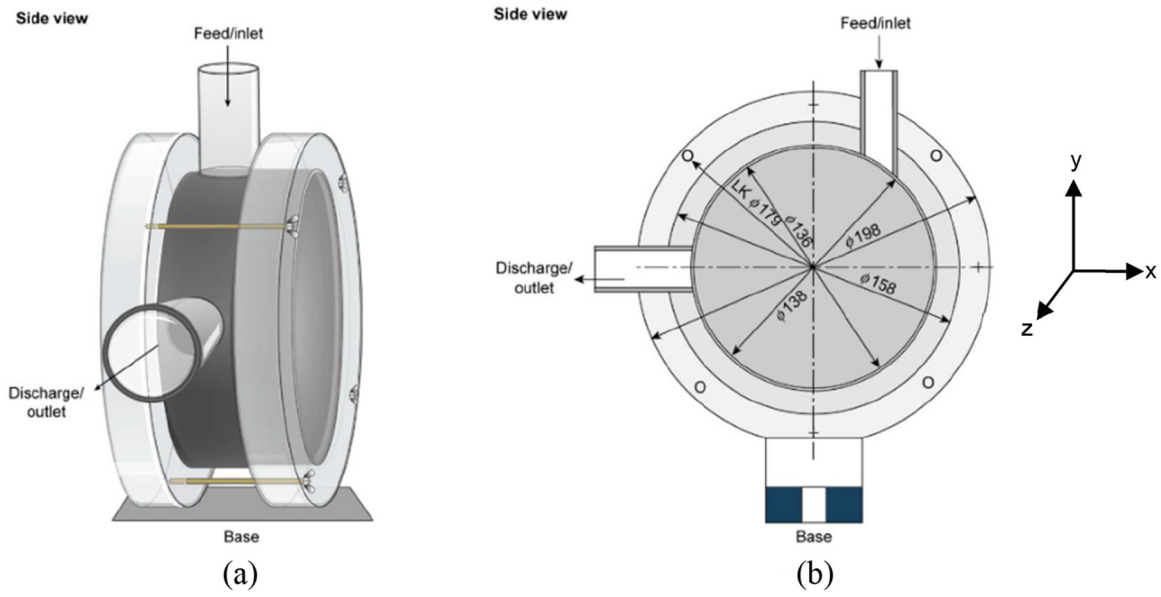

Fig. 1. Schematic illustration of solid model of the flow geometry (not to scale, all dimensions in millimetres) (a) front view (b) side view.

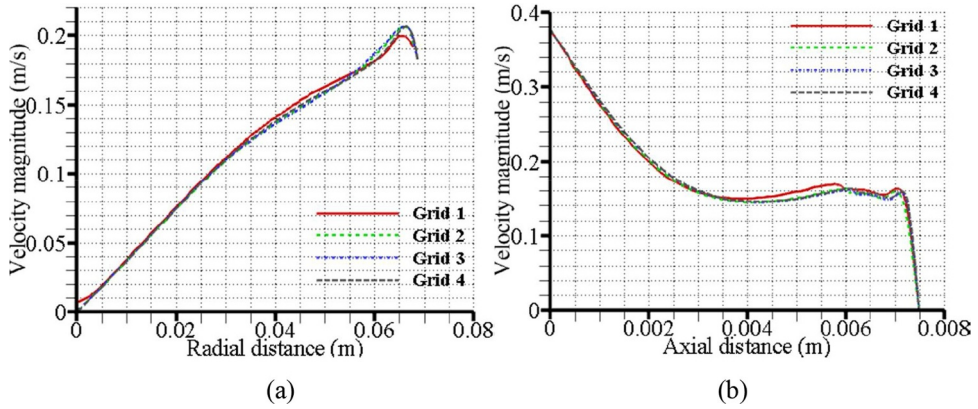

Fig. 2. Flow velocity profiles of different grid sizes on YZ and XZ planes for RNG *k-ε* model N = 70 *rpm* (a) x = 0.003725 (b) y = 0.045.

Table 2
Mesh metrics for the structured hexahedral grid

Mesh number	Nodes	Skewness (average)	Orthogonal quality (average)
Grid 1	51,448	9.30×10^{-2}	0.9893
Grid 2	499,848	5.82×10^{-2}	0.9923
Grid 3	995,180	4.78×10^{-2}	0.9941
Grid 4	1,434,632	4.83×10^{-2}	0.9924

2.2. Discrete Phase Force-Balance Equations

The force balance equation obtained from the Newton's second law that governs the particle acceleration along with the particle translational equation are used to resolve the particle trajectory. This is achieved by stepwise integration of the trajectory equation (Eq. 5) along with any auxiliary equations describing any heat and mass transfer from the discrete phase to the continuous phase, while the particle rotational velocity is obtained by solving an additional ordinary differential equations for particle's angular momentum (Eq. 6) ("ANSYS Fluent Theory Guide 18.2," 2017; Derksen, 2003).

$$m\frac{d\vec{v}}{dt} = \vec{F_D} + \vec{F_P} + \vec{F_{VM}} + \vec{F_G} + \vec{F_B} + \vec{F_L} + \vec{F_{int}} \quad (5)$$

Table 3
Phase properties and numerical simulation parameters

Fluid phase	water	
Density (kgm^{-3})	998	
Dynamic viscosity ($kgm^{-1}s^{-1}$)	8.94×10^{-4}	
Temperature (°C)	25	
Discrete phase	Case 1: Mono-sand	Case 2: Poly-ballotini
Maximum particle size (μm)	-	20
Mean particle sizes (μm)	2, 6, 10	2, 6, 10
Minimum particle size (μm)	-	1
Particle density (kgm^{-3})	2650	2500
Particle shape	Spherical	Spherical
Number of injected particles (-)	3.6×10^6, 7.2×10^6	1.25×10^7, 2.5×10^7
Solids volume fractions (-)	8.2×10^{-6}, 1.6×10^{-5}	8.7×10^{-6}, 1.7×10^{-5}
Particle injection type	Surface	Surface
Total injection time (s)	0.005, 0.01	0.005, 0.01
Phase coupling scheme	One-way	One-way
Mixing speeds (*rpm*)	70 – 130	70 – 130
Particle restitution coefficients (-)	0.20-0.99	0.20-0.99
Wall reflection coefficients (-)	1	1
Friction coefficient (-)	0.2	0.2
Particle tracking time step Δt (s)	1×10^{-4}	1×10^{-4}

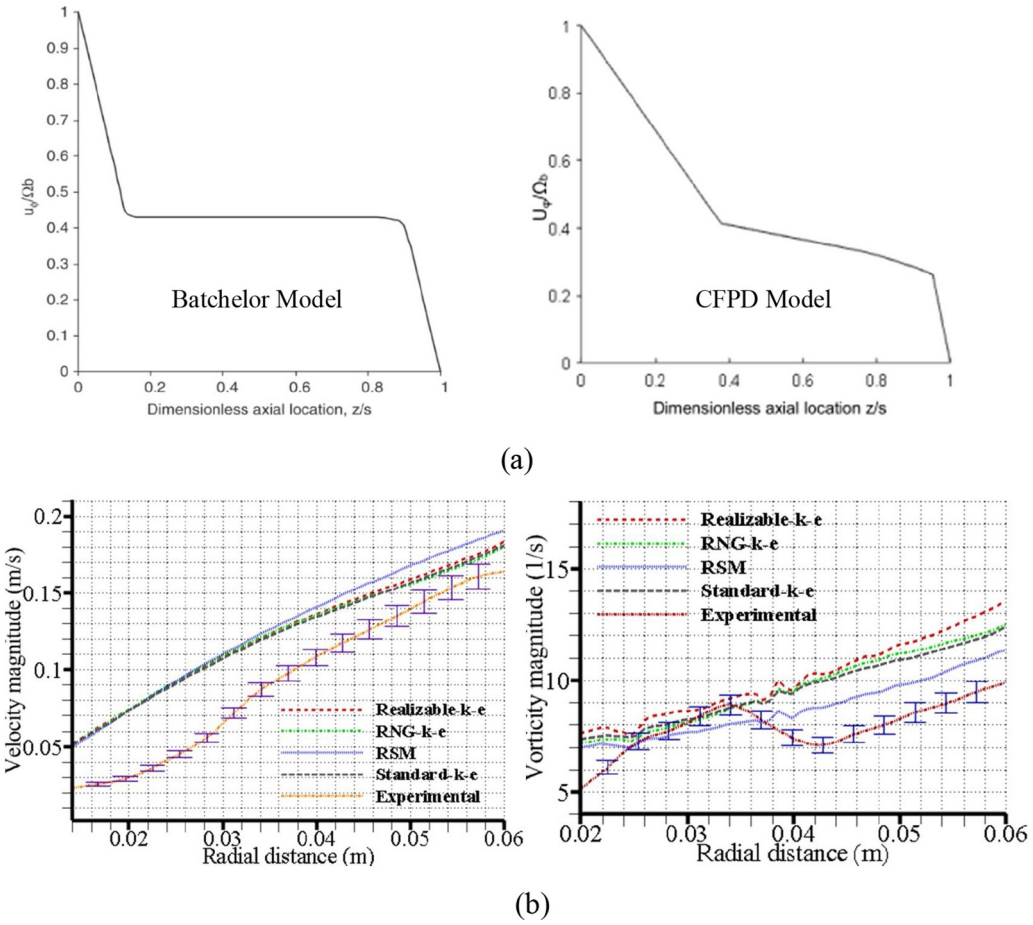

Fig. 3. Vertical and horizontal velocity and vorticity profiles on XZ plane at y = 0.068 and YZ plane at x = 0.003725 (a) horizontal velocity profiles for CFPD and Batchelor model (b) vertical velocity profiles for CFPD model and PIV analysis.

$$I_p \frac{d\vec{\omega}_p}{dt} = \frac{\rho_f}{2}\left(\frac{d_p}{2}\right)^5 C_\omega \vec{\Omega} = \vec{T} \tag{6}$$

where F_D, F_P, F_{VM}, F_G, F_L, F_{int}, represent the drag, pressure gradient, virtual mass, gravitational, lift and the granular interaction forces respectively. However, the gravitational and buoyant forces were neglected in this study due to the rotational nature of the flow while the pressure gradient and virtual mass forces were considered to be important as the ratio of the phase densities is greater than 0.1 ("ANSYS Fluent Theory Guide 18.2," 2017). Other non-contact interfacial forces that mediate particle-particle interactions such as Van der Waals attraction, Born repulsion, electric double layer (EDL), as well as the Basset history and viscous stress forces due to fluid-particle interactions are beyond the scope of this work and were not considered.

2.3. Determination of the Granular Collisional Forces

The granular collision or discrete phase interaction force F_{int} in Eq. 5 is modelled from a correlation derived from the solids phase stress tensor due to the random collisions and translations as a result of fluctuating particle velocities using the kinetic theory of granular flow as follows (Eq. 7) ("ANSYS Fluent User's Guide 18.2," 2017; Cloete et al., 2012; Hashemisohi et al., 2019):

$$F_{int} = -\frac{1}{\rho_s}\nabla\cdot\bar{\bar{\tau}}_s \tag{7}$$

where ρ_s represent the solids density, and $\bar{\bar{\tau}}_s$ is the solids stress tensor which includes the solids pressure, shear stress and normal stress (Cloete et al., 2012). The solids stress tensor is given by Eq. 8 as follows:

$$\bar{\bar{\tau}}_s = -p_s\bar{I} + \alpha_s\mu_s(\nabla\overline{v_s} + (\nabla\overline{v_s})^T) + \alpha_s\left(\lambda_s - \frac{2}{3}\mu_s\right)\nabla\cdot\overline{v_s}\bar{I} \tag{8}$$

where p_s, μ_s, λ_s, are the solids pressure, shear viscosity, and bulk viscosity respectively. The solids pressure which is a measure of the momentum transfer due to the fluctuating motion of particles and their collisions is given by (Eq. 9):

$$p_s = \alpha_s\rho_s\Theta_s + 2\rho_s(1+e_{ss})\alpha_s^2 g_{0,ss}\Theta_s \tag{9}$$

The equation above describes a formulation given by Lun et al. ("ANSYS Fluent Theory Guide 18.2," 2017) in which the first term on the right-hand side represent the kinetic contribution with the second term representing the collisional contribution, while the frictional contribution can be neglected for particle spacing below the packing limit ("ANSYS Fluent Theory Guide 18.2," 2017). The term e_{ss} is the coefficient of restitution for particle-particle collisions, $g_{0,ss}$ is the radial distribution function which is a correlation factor that modifies the probability of collisions when the solid granular phase is close to the packing limit (Eq. 10), while Θ_s is the solids granular temperature which is a measure of the random motion of the particles and it is proportional to the kinetic energy of the fluctuating particle motion. It is defined as one third of the square of the fluctuating particle velocities (Taghizadeh et al., 2018) (Eq. 11). The granular temperature is obtained by solving the algebraic form of the transport equations of the kinetic theory (Eq. 12), in which the convection and diffusion terms in the transport equations are neglected (Cloete et al., 2012; Hashemisohi et al., 2019).

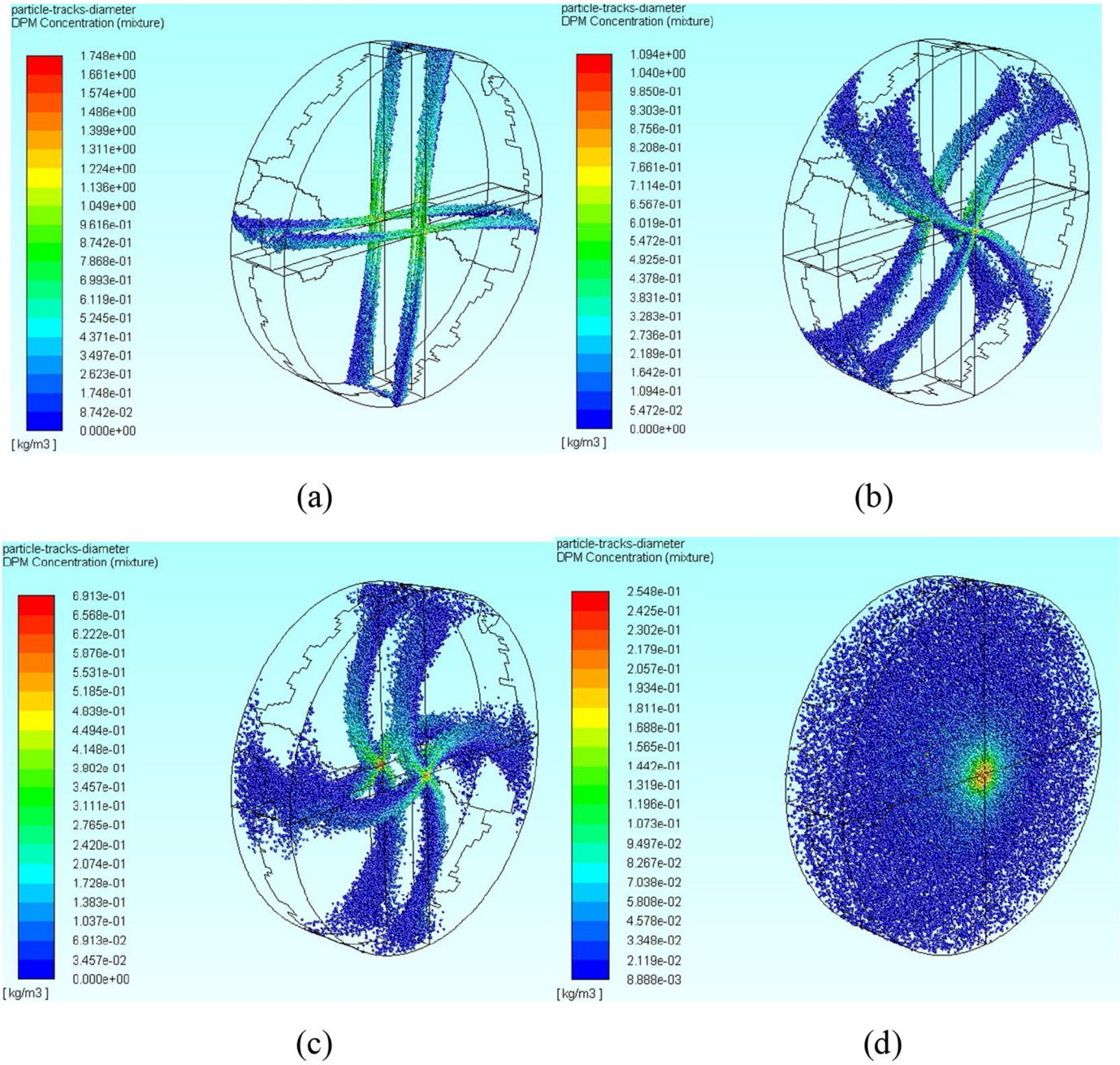

Fig. 4. Spatiotemporal evolution of the instantaneous DPM solids concentration of ballotini particles N = 70 rpm, $e_{ss} = 0.99$, $d_{p,sand} = 10$ μm (a) t = 0.01s (b) t = 0.05s (c) t = 0.1s (d) t = 1s.

$$g_{0,ss} = \left[1 - \left(\frac{\alpha_s}{\alpha_{s,max}}\right)^{\frac{1}{3}}\right]^{-1} \tag{10}$$

$$\Theta_s = \frac{1}{3}(u_{s,i}u_{s,i}) \tag{11}$$

$$\frac{3}{2}\left[\frac{\partial}{\partial t}(\rho_s\alpha_s\Theta_s) + \nabla\cdot(\rho_s\alpha_s\vec{v}_s\Theta_s)\right] = (-p_s\bar{\bar{I}} + \bar{\bar{\tau}}_s):\nabla\vec{v}_s + \nabla\cdot(k_{\Theta_s}\nabla\Theta_s - \gamma_{\Theta_s} + \varphi_{ls}) \tag{12}$$

The solids stress which is composed of the shear viscosity due to the kinetic motion $\mu_{s,kin}$, collisional interactions $\mu_{s,col}$ and frictional particle interactions $\mu_{s,fr}$ (Lun et al. and Gidaspow et al. ("ANSYS Fluent Theory Guide 18.2," 2017)) given in Eqs. 13-14 and the bulk viscosity which account for the particle resistance to expansion and compression (Lun et al. ("ANSYS Fluent Theory Guide 18.2," 2017)) are given in Eq. 15 ("ANSYS Fluent Theory Guide 18.2," 2017). The frictional contribution to the shear viscosity can be neglected in Eq. 14 for dilute flows below the packing limit.

$$\mu_s = \mu_{s,col} + \mu_{s,kin} + \mu_{s,fr} \tag{13}$$

$$\mu_s = \frac{4}{5}\alpha_s{}^2\rho_s d_s g_{0,ss}(1+e_{ss})\left(\frac{\Theta_s}{\pi}\right)^{\frac{1}{2}} + \frac{10\rho_s d_s\sqrt{\Theta_s\pi}}{96\alpha_s(1+e_{ss})g_{0,ss}}\left[1 + \frac{4}{5}g_{0,ss}\alpha_s(1+e_{ss})\right]^2 \tag{14}$$

$$\lambda_s = \frac{4}{3}\alpha_s\rho_s d_s g_{0,ss}(1+e_{ss})\left(\frac{\Theta_s}{\pi}\right)^{\frac{1}{2}} \tag{15}$$

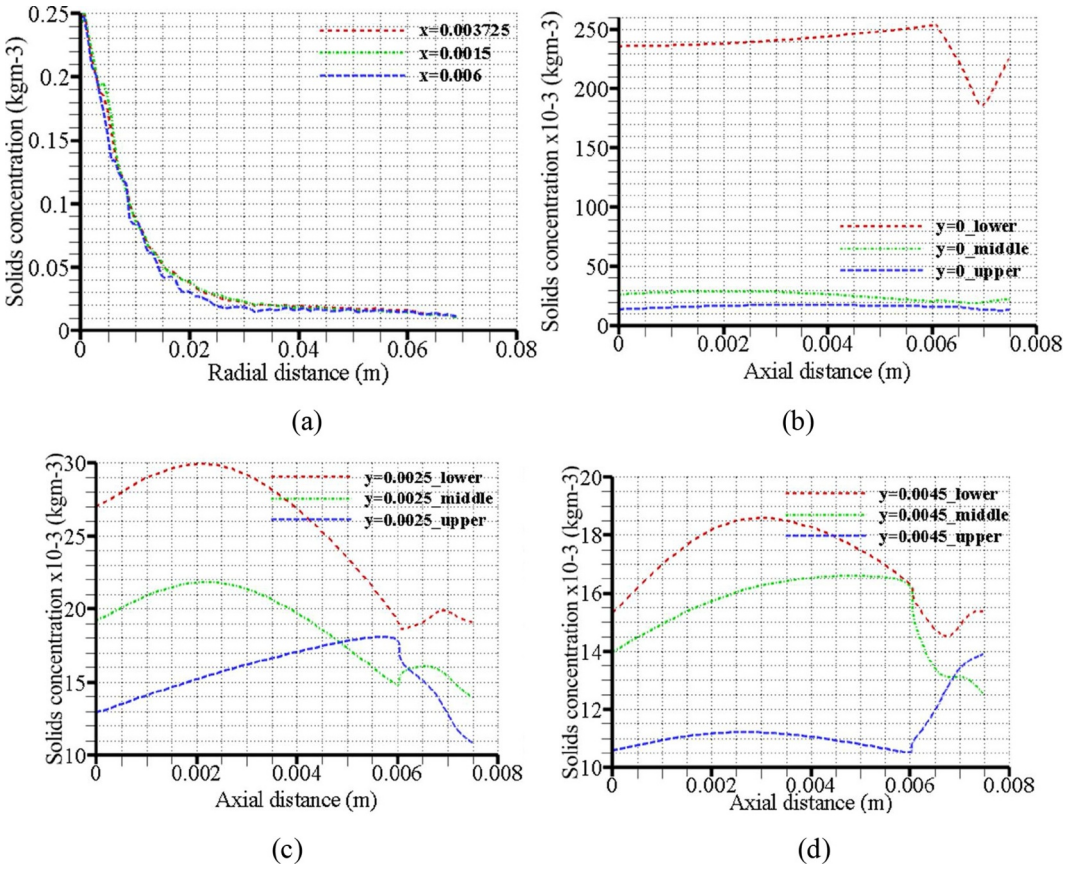

Fig. 5. Vertical and horizontal profiles of the instantaneous DPM solids concentration of ballotini particles on YZ and XZ planes after 1s N = 70 *rpm*, $e_{ss} = 0.99$, $d_{50,ballotini} = 10$ μm (a) vertical profiles (b) horizontal profile y = 0 (c) horizontal profile y = 0.025 (d) horizontal profile y = 0.045.

2.4. Turbulent Dispersion of Particles

The effect of the turbulent continuous phase flow on the discrete phase dispersion can be determined using the stochastic tracking or deterministic method. The discrete random walk (DRW) formulation is available in ANSYS Fluent. This stochastic method based on the eddy lifetime approach incorporates the influence of turbulent velocity fluctuations on the particle trajectories by deriving the fluctuating velocity *u'* part of the instantaneous velocity *u* via a Gaussian distribution function where σ refers to the *rms* value of the fluctuating velocity *u'*. These derivations are given in Eqs 16-17 where ζ is a vector formed by normally distributed random number, *k* is the kinetic energy, and *σ* is the root mean square value of the fluctuating velocity with the assumption of an isotropic turbulence (Greifzu et al., 2016).

$$u' = \zeta\sigma \tag{16}$$

$$\sigma = \sqrt{\frac{2k}{3}} \tag{17}$$

2.5. Turbulence Modelling and Drag Modifications

The *k-ε* dispersed turbulence model is used to account for the effect of turbulence on the multiphase flow by calculating the Reynolds stress tensor using an extended form of the single phase RNG-*k-ε* two-equation model with curvature correction to improve the turbulence predictions due to the rotational nature of the flow ("ANSYS Fluent Theory Guide 18.2," 2017). Using a modified form of *k-ε* model transport equations (Eqs. 18-19, the turbulence predictions are obtained for the continuous phase while turbulence quantities for the dispersed phase are given in terms of the mean characteristics of the continuous phase and the ratio of the particle relaxation time and the eddy-particle interaction time from Tchen-theory (Wadnerka et al., 2012; "ANSYS Fluent Theory Guide 18.2," 2017). The effect of increasing turbulence (Reynolds number and eddy sizes) on the drag predictions was accounted for by using a drag modification factor proposed by Brucato et al. (Wadnerka et al., 2012) which expresses drag coefficient as a function of the ratio of particle diameter and Kolmogorov length scale (Eq. 20) (Wadnerka et al., 2012). However, the effect of the Magnus rotational lift force of the fluid was not taken into account in coupled DPM calculations due to the limitations in the numerical code. Therefore particle rotation was only considered from the torque on the particle arising particle-wall interactions in the coupled calculations ("ANSYS Fluent User's Guide 18.2," 2017). Turbulence damping, modulation or attenuation by the suspended particles especially at high solids loadings may also be incorporated into the model by implementing a two-way turbulence coupling in the numerical simulations using the formulation proposed by Amsden, O'Rourke and Faeth (Balachandar and Eaton, 2009).

$$\frac{\partial}{\partial t}(\alpha\rho k) + \nabla\cdot(\alpha\rho\vec{U}k) = \nabla\cdot\left(\alpha\left(\mu + \frac{\mu_t}{\alpha_k}\right)\nabla k\right) + \alpha G - \alpha\rho\varepsilon + \alpha\rho\Pi \tag{18}$$

and

$$\frac{\partial}{\partial t}(\alpha\rho k) + \nabla\cdot(\alpha\rho\vec{U}\varepsilon) = \nabla\cdot\left(\alpha\left(\mu + \frac{\mu_t}{\sigma_k}\right)\nabla\varepsilon\right) + \alpha\frac{\varepsilon}{k}(C_{1\varepsilon}G - C_{2\varepsilon}\rho\varepsilon) + \alpha\rho\Pi \tag{19}$$

$$\eta = 1 + \left(\frac{C_D - C_{D0}}{C_{D0}}\right) = K\left(\frac{d_p}{\lambda}\right)^3 \tag{20}$$

where C_D is the computed drag coefficient due to the turbulence effect,

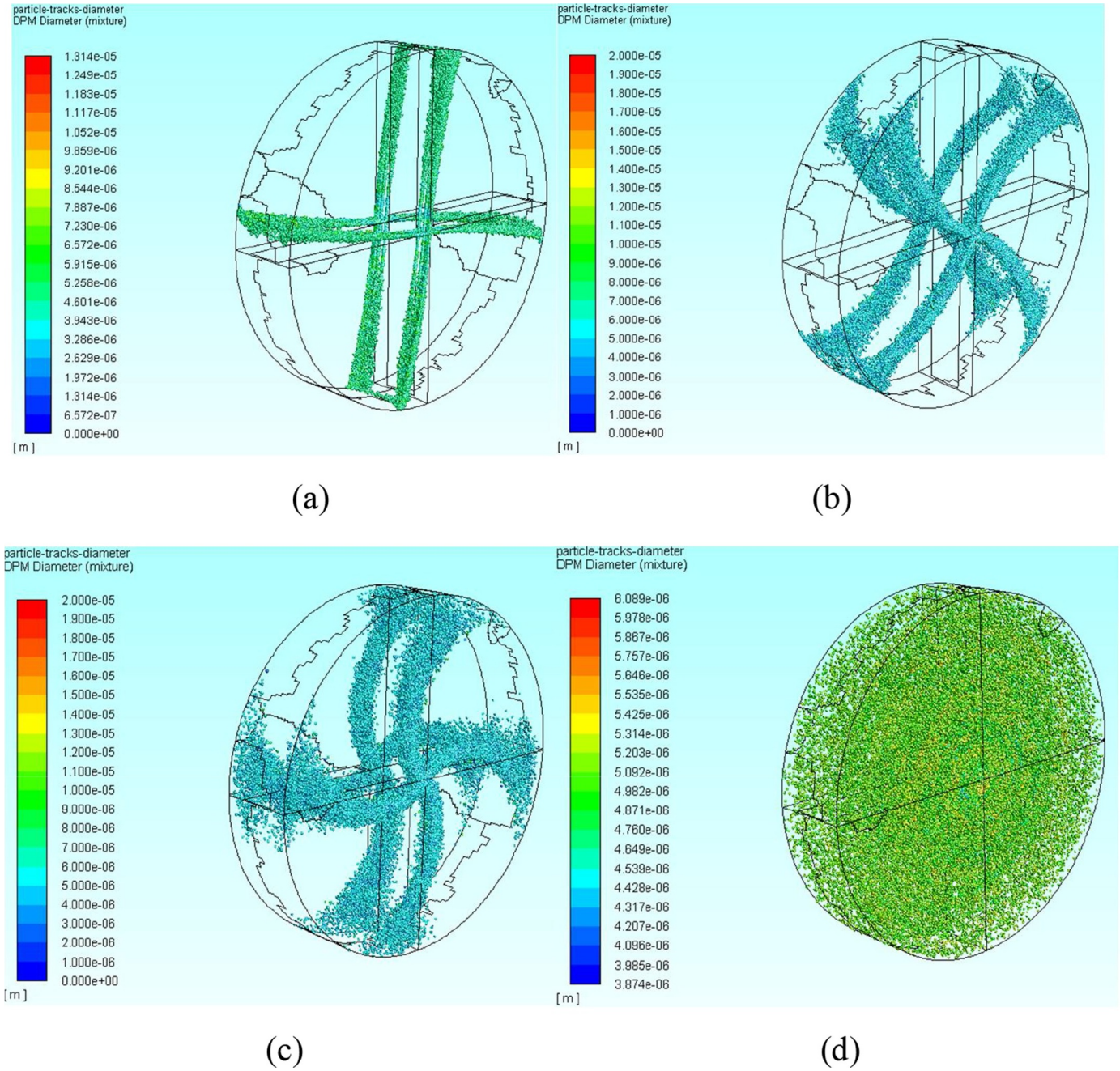

Fig. 6. Spatiotemporal evolution of the instantaneous DPM particle sizes of ballotini particle N = 70 *rpm*, $e_{ss} = 0.99$, $d_{50,ballotini} = 10$ μm (a) t = 0.01s (b) t = 0.05s (c) t = 0.1s (d) t = 1s.

C_{D0} is the drag coefficient without turbulence modification, K is a constant with value of 6.5×10^{-6}, d_p is the particle diameter, and λ is Kolmogorov length scale ("ANSYS Fluent Theory Guide 18.2," 2017; Wadnerka et al., 2012). In addition to the stresses predicted by the kinetic theory, the KTGF model may be extended by include the frictional effect of the granular phase when the solids volume fraction exceeds the critical value using the frictional stress model (FSM) which incorporate frictional viscosity and frictional pressure terms in Eqs. 9 and 14 ("ANSYS Fluent Theory Guide 18.2," 2017). The DDPM form of Eqs. 1-2 is used when dispersed phase is close to the packing limit especially in the case of dense particulate flows. These two additional equations are however omitted from this investigation due to the dilute nature of the flow considered. However, these parameters may be included depending on the flow scenario being modelled ("ANSYS Fluent Theory Guide 18.2," 2017). Table 1 gives a summary of the KTGF and DPM force models and governing equations used in the implementation of the numerical calculations.

3. Implementation of the Numerical Solution

3.1. Flow domain and geometry

A bench-scale rotor-stator vortex reactor for the agglomeration of dilute particulate suspension which was developed in-house was employed in carrying out this study. Detailed information on the reactor setup and the process conditions can be found in our previous communications (Oyegbile et al., 2017, 2018). The geometric design of the reactor and subsequent mesh generation of the flow domain are briefly presented. In implementing a numerical scheme to solve the above set of equations describing the particle-particle, particle-wall and fluid-

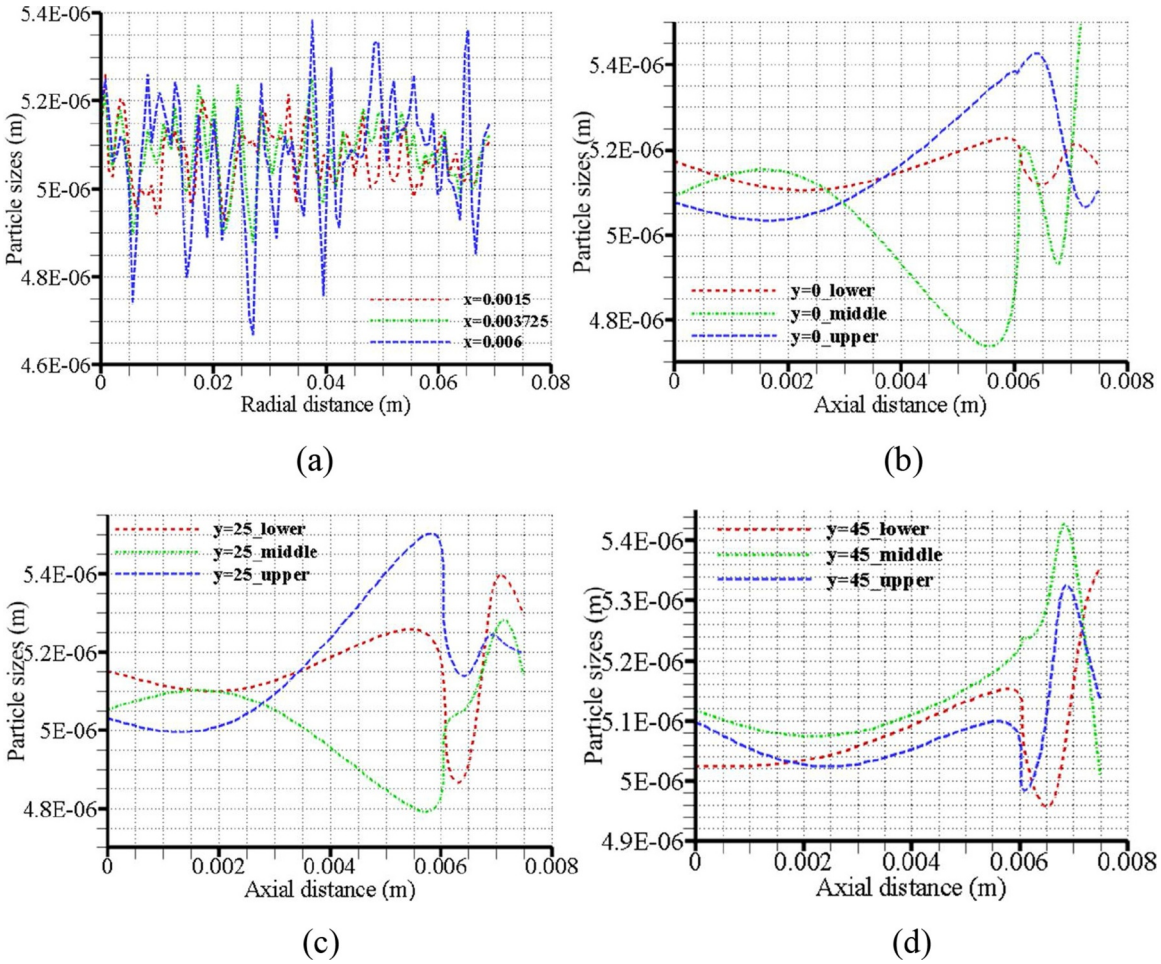

Fig. 7. Vertical and horizontal profiles of the instantaneous DPM size distribution of ballotini particles on the YZ and XZ planes after 1s N = 70 *rpm*, $e_{ss} = 0.99$, $d_{50,ballotini} = 10$ μm (a) vertical profiles (b) horizontal profile y = 0 (c) horizontal profile y = 0.025 (d) horizontal profile y = 0.045.

particle interactions within the reactor, a solid model of the reactor depicted schematically in Figure 1 was first created using a commercial solid modelling software (ANSYS Spaceclaim 18.2, ANSYS Inc.).

3.2. Fluid flow description and PIV measurements

The flow within the reactor is an enclosed Batchelor flow which is an axis-symmetrical forced vortex flow with separated boundary layers at the rotor and the stator and a radially pumping flow towards the stator. Particle dispersion within the reactor is largely shear driven with patches of turbulence especially above the critical disc or local rotational Reynolds number. Batchelor proposed a model to describe the fluid flow structure in an enclosed rotor-stator disc system with the fluid being pumped axially outwards from the rotor boundary layer (Childs, 2011). Characterization of the flow dynamics was carried out via a Particle Image Velocimetry (PIV) analysis. The details of the PIV flow measurements are available elsewhere (Oyegbile et al., 2017). For the sake of brevity, the discussion will focus on the description of the flow tracing particles which consists of a mixture of hollow glass spheres and silver-coated glass spheres in ratio 1:1 with a median diameter of 10μm supplied Dantec Dynamics A/S, Denmark. The particles were selected due to their good scattering efficiency and sufficiently small velocity lag (Oyegbile et al., 2017).

3.3. Solution control and grid independence analysis

Four different grid sizes were generated using the ANSYS Meshing software, after which a sensitivity analysis was performed to determine an optimal grid size. Thereafter, a high-quality hexahedral mesh of approximately 431,000 cells (mesh 2) was selected for the numerical simulation based on the sensitivity analysis shown in Fig. 2. Table 2 gives a quantitative metrics of the mesh quality for all the grid sizes considered. Monodispersed sand and polydispersed ballotini particles were selected as model granular materials for the particle tracking calculations. They were selected because they give a realistic representation of real-world particulate systems. The mesh sensitivity study was conducted by carrying out the numerical simulation on successively finer grids using four different mesh resolutions. Thereafter, the results of the tangential velocities on selected planes within the flow domain along the axis of rotation were compared for all the grids to establish their grid independence. Finally, a mesh resolution of 431,000 hexahedral cells was chosen to run the simulation to a converged solution based on the fact that the relative errors between the mesh sizes were quite minimal (below 1% difference). This optimized mesh was thereafter employed for subsequent computations of all flow properties. The residuals, moment and average kinetic energy are used as the convergence parameters for the numerical calculations while the solution is considered to have converged when the residual reduces to an acceptable level of 1×10^{-3}. All numerical simulations were performed using a quad-core i5-6500, 3.20 GHz 6MB cache CPU with 32 GB RAM while the other simulation parameters are given in Table 3. Figure 2 shows the vertical and horizontal tangential velocity profiles for all the four grids employed for the sensitivity analysis. The profiles were drawn along the YZ and XZ planes at $x = 0.003725$ and $y = 0.045$, respectively for a rotation speed of 70 rpm.

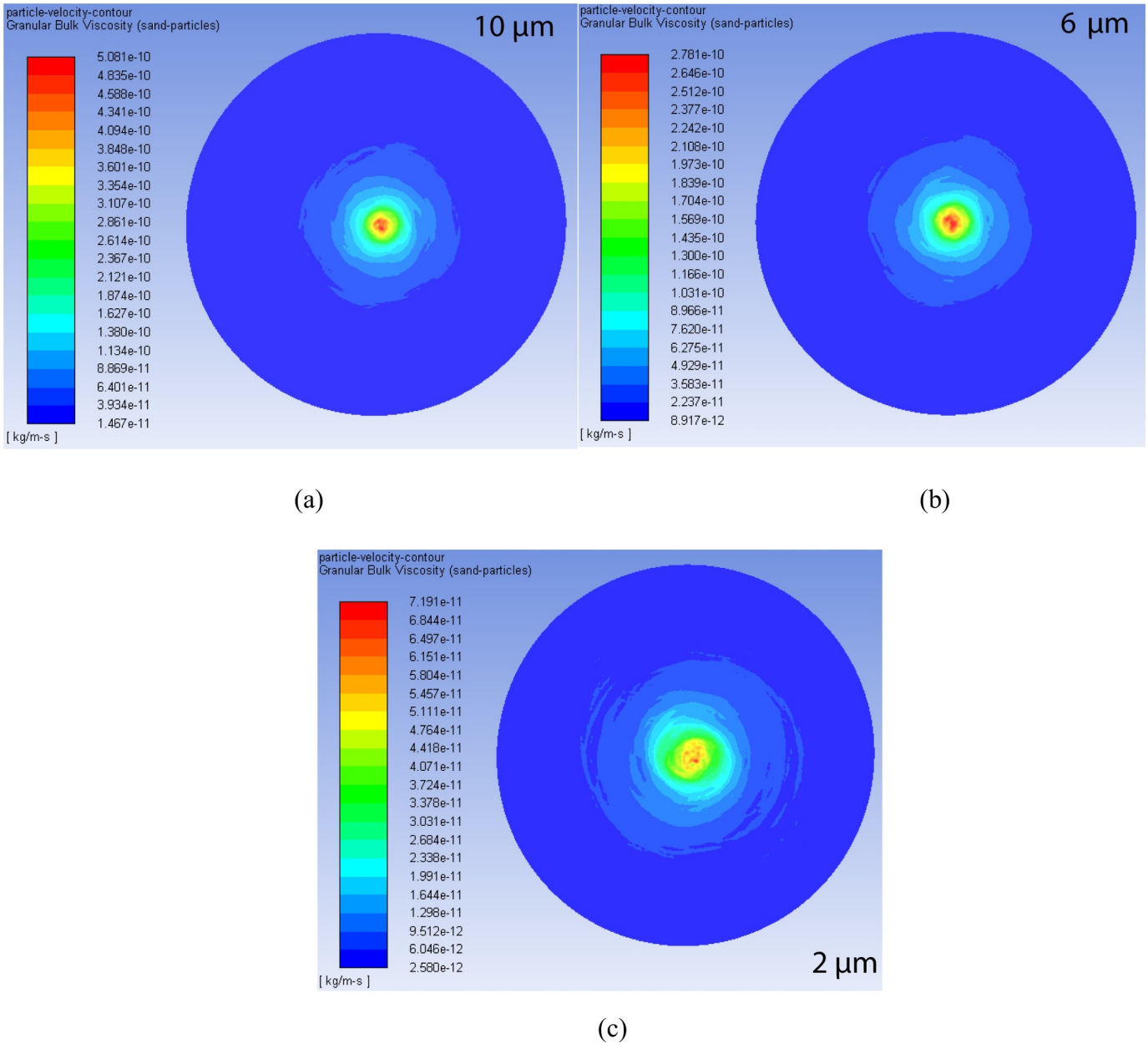

Fig. 8. Contours of granular bulk viscosities of sand particles on YZ plane after 1s for different particle sizes x = 0.0015, e_{ss} = 0.99, N = 70 rpm (a) 10 µm (b) 6 µm (c) 2 µm.

3.4. Numerical solution strategy and boundary conditions

In this work, a 3D CFPD model was developed to predict the fluid-particle interactions in a bench-scale vortex reactor using point-particle method where moving particles are treated as mass points. In this so-called hard-sphere or event-driven approach, some abstractions are made regarding the particle shape, volume and fluid flow around the particles (Greifzu et al., 2016; Li et al., 2015). The turbulent fluid flow was modelled by solving incompressible RANS equations with scalable wall functions, while the discrete phase was modelled using coupled DPM-KTGF Lagrangian particle tracking equations, both of which were implemented in a commercial CFD software package (ANSYS Fluent 18.2, ANSYS Inc.) A converged steady-state fluid flow field was weakly coupled to a transient DPM particle tracking model via a one-way coupling to account for the fluid-particle interactions and specie distribution within the flow domain. This was achieved by increasing the number of continuous phase calculations between the trajectory calculations after a converged steady-state solution has been obtained. A one-way coupling is justified in the present study considering that the mass loadings and volume fractions are quite low at less than 10% and 10^{-4} respectively, and the mean particle sizes are much less than the Kolmogorov length scale ≈ 12µm ("ANSYS Fluent User's Guide 18.2," 2017; Greifzu et al., 2016; Hobbs, 2004). This implies that the discrete phase is primarily influenced by the hydrodynamics of the continuous phase.

The calculation of the particle-particle contact forces was not explicitly resolved but modelled via KTGF. However, this event-driven approach takes into account the energy dissipation and resultant loss of momentum during collisions through the use of restitution coefficients. Gidaspow model was employed to compute the collisional and kinetic viscosities while a formulation by Lun. et al. ("ANSYS Fluent Theory Guide 18.2," 2017) was used for the solids pressure (Eqs. 9, 13 and 14, respectively) (Taghizadeh et al., 2018). Calculations of the particle trajectories was done via a stepwise integration of the trajectory

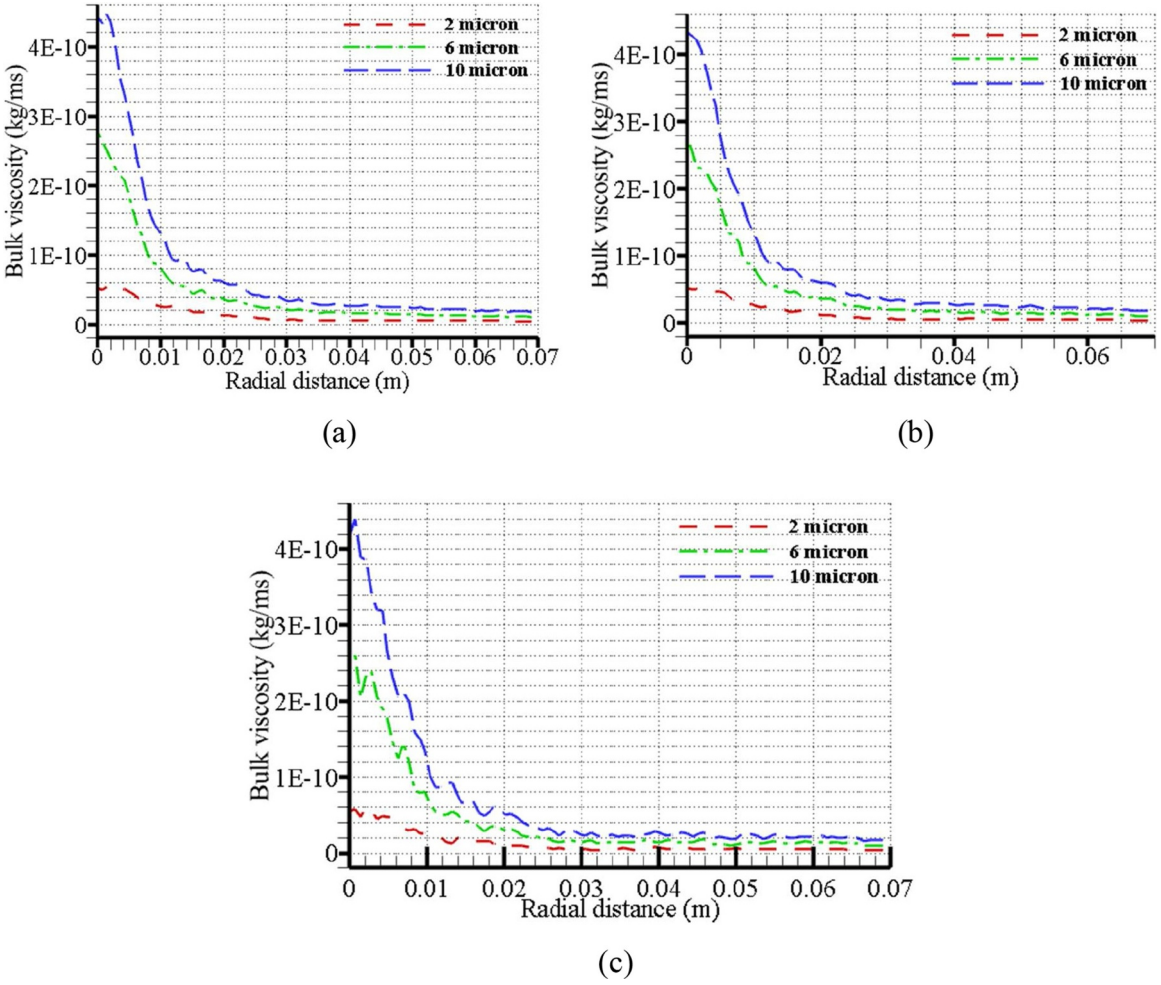

Fig. 9. Bulk viscosity of sand particles as a function of radial distance for different particle sizes on the YZ planes after 1s $e_{ss} = 0.99$ (a) x = 0.0015 (b) x = 0.003725 (c) x = 0.006.

equations from the converged CFD velocity field using an implicit integration scheme (Gannt and Gatzke, 2006; Li et al., 2015). In these idealized particle-particle interactions, particles were injected from surfaces within the reactor wheelspace in the direction of the flow. A reflect type discrete phase boundary condition was imposed on all the walls with no-slip boundary condition for the continuous phase (Wadnerkar et al., 2016). Realistic values of the normal particle restitution and wall reflection coefficients were chosen for the normal forces, while the tangential linear velocity after collision or reflection is function of the linear velocity and the angular velocity due to particle rotation. However, in situations where the particle rotation is not enabled or compatible with the trajectory calculations such as in the case of moving reference frame, a formulation by Tsuji et al. was employed to determine the values of tangential or sliding force with default values used for the friction coefficients ("ANSYS Fluent Theory Guide 18.2," 2017). The default values of the friction coefficient as well as the restitution coefficients specified in Table 3 ensure that the particles retain much of their momentum in the normal and tangential direction after collision. The angular momentum in the wall normal direction is not affected by particle-wall collision which results in an unchanging particle angular velocity in the case of adhesive impact considered in this study ("ANSYS Fluent Theory Guide 18.2," 2017). The coupled algorithm was used for the pressure-velocity coupling while QUICK scheme was applied to the rest of the flow variables. Table 3 shows a summary of the phase properties and the particle injection schemes for the DPM calculations.

3.5. Theoretical and Experimental Validation of the CFPD Model

The validation of the numerical model from this study was done based on the theoretical analysis of the rotor-stator flow or the so-called Batchelor model predictions as well as the PIV flow measurements for the single-phase flow (Figs. 3a and 3b) (Childs, 2011; Oyegbile et al., 2017). Figure 3a shows the Batchelor and the CFPD models' horizontal velocity profiles with two identical separated boundary layers on the rotor and the stator and a middle fluid rotating core. However, the gap ratio used in the Batchelor measurements was quite different from the one used in the present study which might be responsible for the variations observed in the fluid rotating core (Bodnár et al., 2017). Figure 3b shows the vertical velocity and vorticity profiles, which gives a reasonably good agreement between the CFPD model and PIV measurements. Owing to some of the limitations reported in the PIV measurements (Oyegbile et al., 2017), it could be argued that the flow parameters were under-predicted by the PIV analysis. Therefore, the observed deviations were mainly due to some of the experimental limitations rather than the robustness of the CFPD model or the numerical code.

4. Results and Discussion

4.1. Evolution of the Flow Pattern and Discrete Phase Properties

4.1.1. Evolution of the discrete phase concentration

The spatiotemporal evolution of the flow properties in terms of the

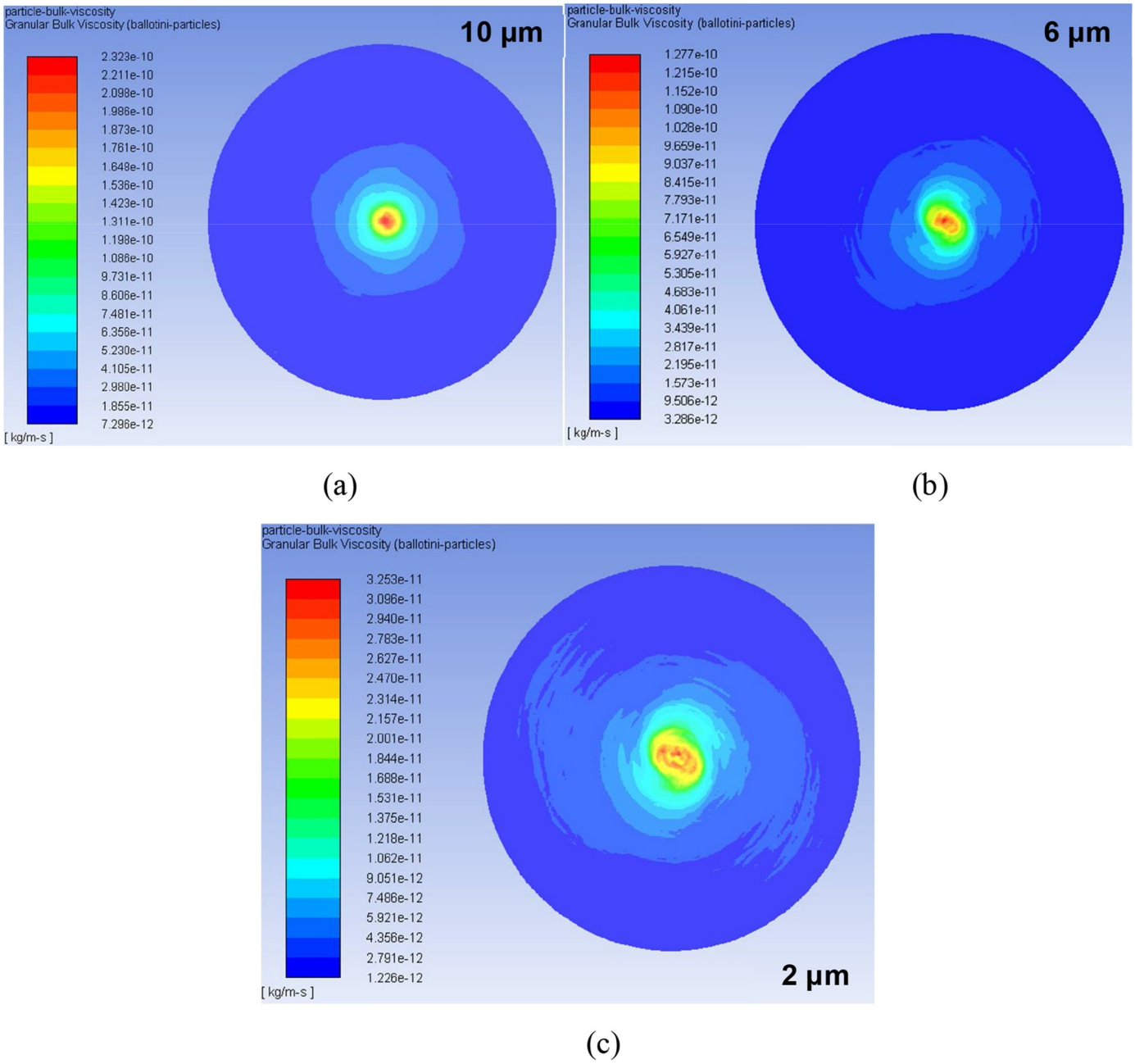

Fig. 10. Contours of granular bulk viscosities of ballotini particles on YZ plane after 1s for different particle sizes x = 0.0015, e_{ss} = 0.99, N = 70 rpm (a) 10 µm (b) 6 µm (c) 2 µm.

discrete phase solids concentration for the poly-dispersed ballotini particles is presented in Figures 4 and 5. It could be observed from the figures that there is an accumulation of higher particle concentration near the rotating shaft similar to the conventional stirred tank at a vertical plane along the impeller (Xie and Luo, 2018). This trend is seen to be consistent and increases throughout the duration of the particle tracking. The area around the shaft does not seem to promote particle mixing as a significant particle holdup was observed in this area due to low turbulence intensity. One way to improve particle mixing in this region is by incorporating baffles or blades into the design of the rotating shaft to promote mixing in this region.

4.1.2. Evolution of the discrete phase size distribution

The spatial and temporal evolution of the particle dispersity and size distribution is presented in Figures 6 and 7 which clearly show a sustained change in the particle dispersity with the tracking time. A nearly uniform particle dispersity with somewhat narrow distribution is observed after 1s due to the onset of steady-state conditions after this period. Steady-state conditions can also be achieved due to an equilibrium of particle collisions, coalescence, growth, breakage and re-agglomeration (Chaumeil and Crapper, 2014; Xie and Luo, 2018). However, this was not investigated in this study. In terms of the spatial distribution, there is a wider particle size distribution axially towards the reactor stator (Figs. 7b-c), while there appears to be a fairly uniform radial distribution of the particle sizes across the reactor diameter (Fig. 7a). The wider particle size distribution observed axially towards the stator might be attributed to the pumping effect of the Batchelor flow in the this direction (Childs, 2011).

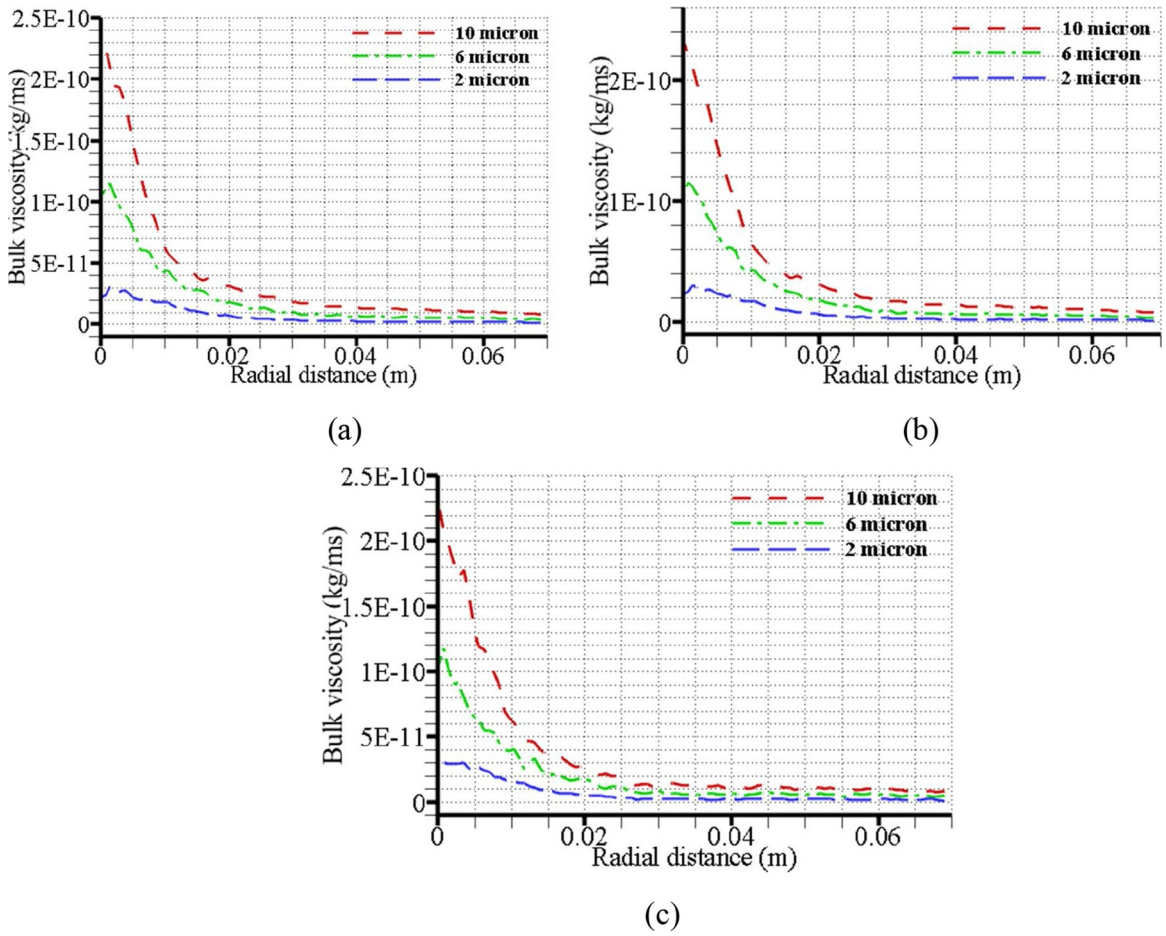

Fig. 11. Bulk viscosity of ballotini particles as a function of radial distance for different mean particle sizes on the YZ planes after 1s $e_{ss} = 0.99$ (a) x = 0.0015 (b) x = 0.003725 (c) x = 0.006.

4.2. Influence of the Operating Conditions on the Granular Properties

4.2.1. The effect of particle size and dispersity on the bulk viscosity

In order to understand the influence of the particle sizes and particle dispersity on the granular properties, numerical simulations were carried out with varying particle sizes starting with the converged solution for the largest particle size to study the effect of different particle sizes on the granular bulk viscosity. Figures 8-9 and Figures 10-11 show the solids bulk viscosity contours and profiles computed at three points along the reactor cavity namely: near the rotor, at the centre and near the stator for mono-dispersed sand and poly-dispersed ballotini particles, respectively. It is observed that the bulk viscosity, which is a function of particle diameter (Eq. 15), increases with the particle sizes and this trend is consistent across the cavity (Figs. 8a-c). It can be seen that the highest values of the bulk viscosities are obtained near the rotor due to high particle velocities and concentration at this position as compared to the centre of the cavity and near the stator. The increase in granular bulk viscosities due to the increasing diameter was due to the increasing resistance of the particles to compression and expansion as the surface area increases. This is consistent with similar studies elsewhere and this implies that the changing particle sizes influences the hydrodynamics of the reactor system (Taghizadeh et al., 2018). A similar trend is observed in the case of ballotini particles (Figs. 10-11) which seems to imply that particle dispersity does not seem to have a strong influence on the granular bulk viscosities. Therefore, it can be argued that the granular bulk viscosity is a function of the particle diameters rather than the dispersity of the particles. However, ballotini particles exhibit a lower bulk viscosity when compared to the sand particles which might be due to their lower densities.

4.2.2. The effect of particle restitution coefficients on the granular pressure

In order to investigate the effect of the particle normal restitution coefficients on the solids pressure, numerical experiments were performed at different particle restitution coefficients starting with the converged solution for the highest restitution coefficient. Figure 12 shows the profiles of the granular pressure for different restitution coefficients. The radial distribution of the solids pressure across the reactor diameter shows a region of high granular pressure near the rotating shaft with no significant variation between the restitution coefficients with the exception of the lowest value of the restitution coefficient (e = 0.2). A sharp reduction in the values of the granular pressure with respect to the radial distance were observed close to the shaft of the reactor. While away from this region, there is little or no differences in the values of the granular pressure for all the restitution coefficients. This observation is consistent with the results obtained from the numerical analysis of particle dispersion in stirred tank using two-fluid model (Xie and Luo, 2018). Since the granular pressure at low solids concentration relies primarily on the kinetic mechanism rather than particle-particle collisions (Cloete et al., 2012), this implies that discrete phase velocity does not seem to vary significantly with the restitution coefficients. The observed trend in the solids pressure with respect to the restitution coefficients might be attributed to the dilute nature of the flow under consideration. However, it is worth pointing out that a wider range of restitution coefficients are possible in practice due to particle roughness and lower values of restitution coefficient are often encountered in practical applications. Gant and Gatzke (Gannt and Gatzke, 2006) in their study reported a restitution coefficients in the range of 0-0.33.

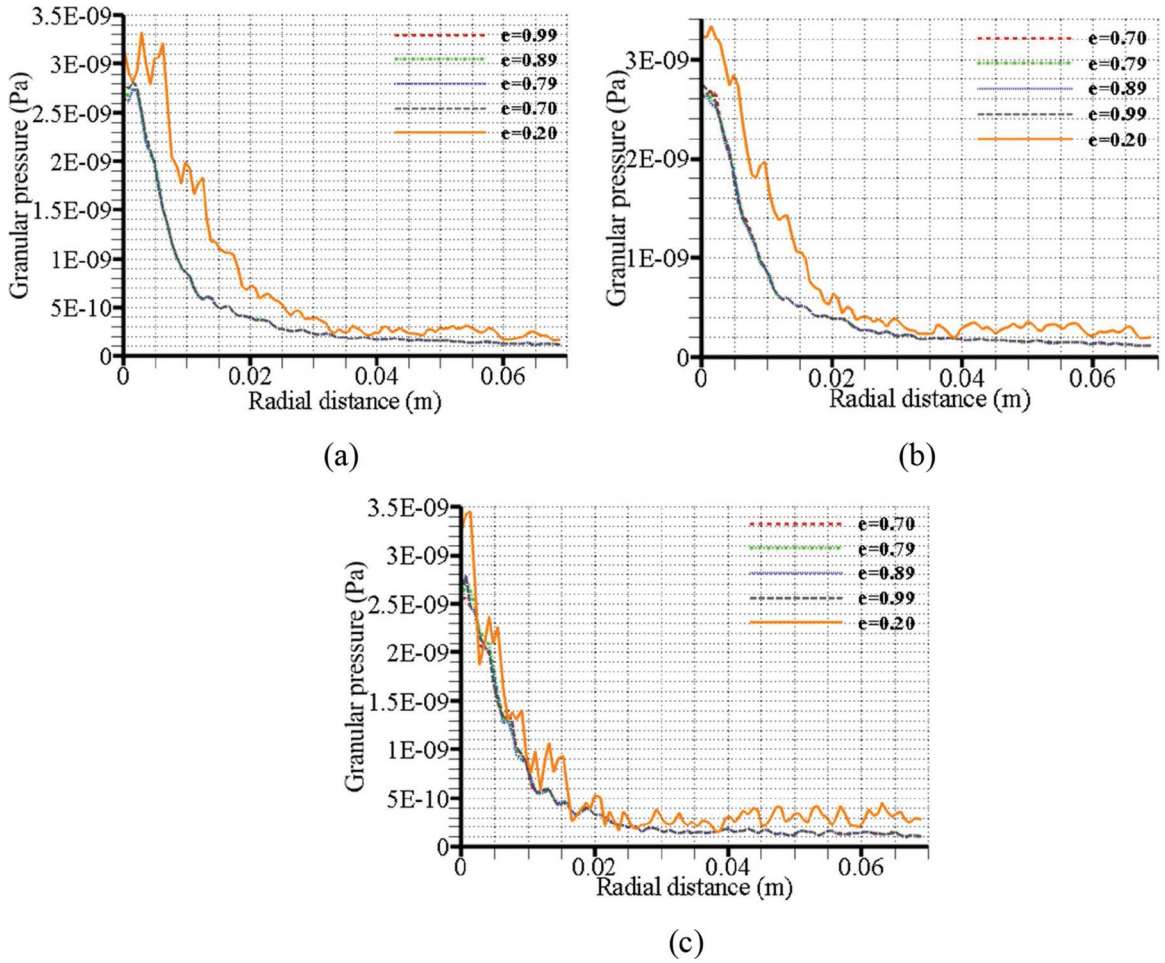

Fig. 12. Granular pressure of sand particles as a function of radial distance for different particle restitution coefficients on the YZ planes after 1s N = 70 *rpm,* $d_{p,sand}$ = 5 μm (a) x = 0.0015 (b) x = 0.003725 (c) x = 0.006.

4.2.3. The effect of the rotation speeds on the granular pressure

In assessing the effect of the reactor rotational speed on the granular properties, numerical simulations were performed at different operating speeds starting with the converged solution for the lowest operating speed of 70 rpm and gradually increasing the speed to the desired values. This is done to ensure stability of the numerical solution ("ANSYS Fluent User's Guide 18.2," 2017). Figure 13 shows the influence of the rotational speed on the spatial distribution of the granular pressure. In terms of the temporal evolution of the solids pressure, a gradual reduction in its absolute values was observed on the YZ plane near the rotor as the particle tracking time increases and with the simulation approaching steady-state condition. The spatial distribution of the granular pressure shows a consistent trend of high solids pressure around the shaft. This high solids pressure in this region might be due to the higher solids concentration in the area around the shaft resulting in a higher collisional contributions to the solids pressure (Cloete et al., 2012). The granular pressure in terms of the absolute values seem to correlate with higher rotational speed in the region near the rotating shaft. However, away from this region, the solids pressure does not seem to vary significantly with the operating speed. One possible reason for this observation might be the reduced collisional effects due to lower solids concentration away from the shaft. One way to improve the homogeneity of the solids distribution is to incorporate baffles into this region to increase the vorticity, turbulence intensity and consequently, the particle dispersion.

5. Conclusions

A coupled DPM-KTGF hybrid model was developed to study the interactions of granular materials within an enclosed Batchelor flow. The CFPD model was employed to predict the spatiotemporal properties of the discrete particles as well as the flow characteristics using an in-house vortex reactor designed for the agglomeration of particles in dillute suspensions. Based on the findings of this study, the following conclusions were made:

- There is a spatiotemporal variation in the discrete phase concentration and particle size distribution (PSD) within the reactor, with higher particle concentration in the region around the shaft and a fairly uniform spatial distribution of the particle sizes elsewhere.
- The granular bulk viscosity in terms of the absolute values exhibit a positive correlation with the particle sizes with increasing particle sizes resulting in higher bulk viscosities.
- The particle dispersity does not have any significant effect on the granular bulk viscosities. This implies that the granular bulk viscosity is a function of the particle diameters rather than the dispersity of the particles.
- The restitution coefficients and the rotational speeds do not significantly influence the granular properties beyond the area close to the rotating shaft due to low turbulence intensity causing high solids hold up in this region.
- The granular pressure in terms of the absolute values have a positive correlation with higher rotational speed especially near the rotating

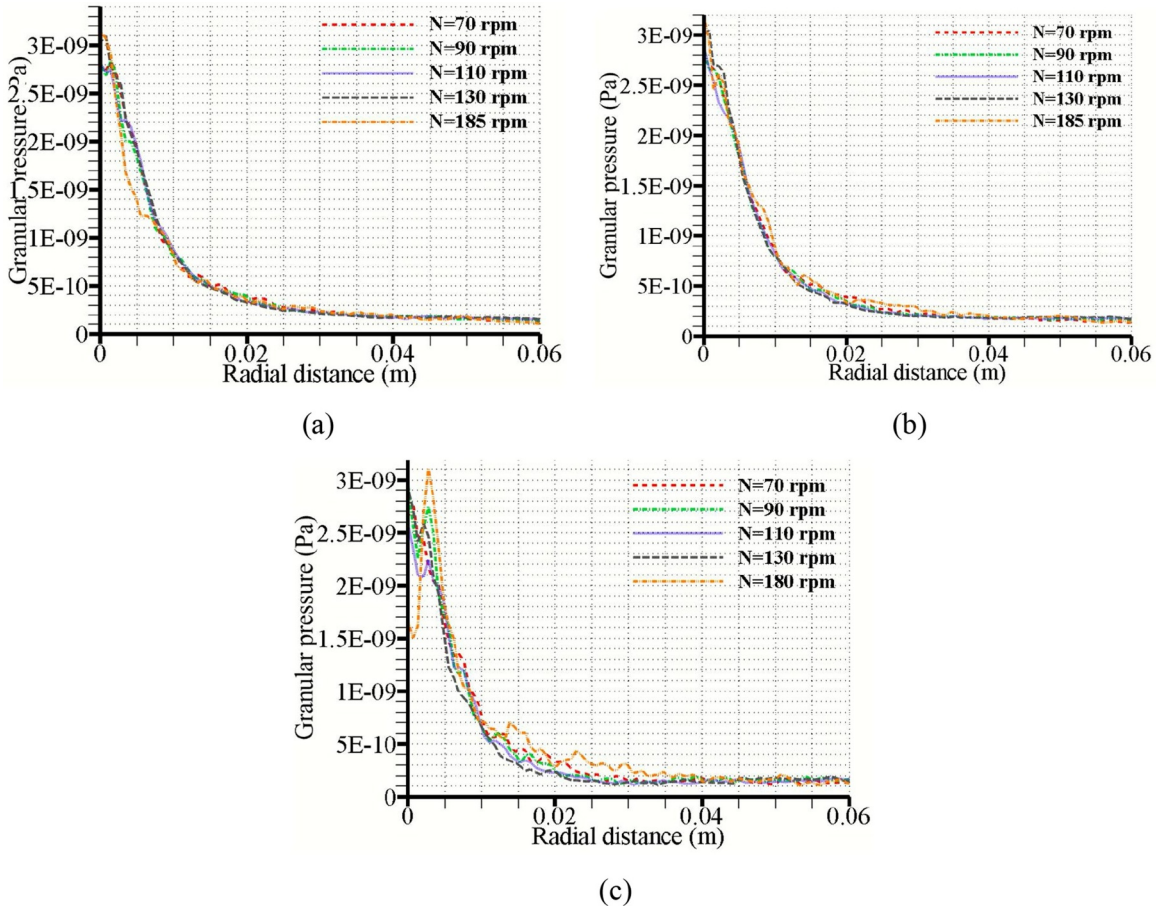

Fig. 13. Granular pressure of sand particles as a function of radial distance for different rotation speeds on the YZ planes after 1s $e_{ss} = 0.99$, $d_{p,sand} = 10$ μm (a) x = 0.0015 (b) x = 0.003725 (c) x = 0.006.

shaft. However, away from this region, the solids pressure does not vary significantly with the operating speed.

- The granular pressure at low solids concentration relies primarily on the kinetic mechanism rather than particle-particle collisions which implies that discrete phase velocity does not vary significantly with the restitution coefficients especially at low solids loading.
- The vertical velocity and vorticity profiles within the reactor give a reasonably good agreement between the CFPD model predictions and PIV measurements. The minor difference between CFPD model and PIV measurements was due to the fact that some of the flow parameters were under-predicted by the PIV analysis.

Furthermore, the current CFPD model might be extended to include other non-contact interparticle forces. Therefore, future work will focus on the extension of this model to other non-contact forces as well as other fluid-particle forces which were not considered in the present investigation using the square-well approach presented by Weber and Hrenya (Weber and Hrenya, 2006) or by full coupling of the flow field to the DEM model. It will also be interesting to study the full mechanisms of fluid-particle, particle-particle and particle-wall interactions leading to particle collisions, coalescence/aggregation, growth and breakage and compare the results of this fully resolved approach to the present investigation. For instance, the full DEM simulations can be used to develop constitutive models to improve the KTGF model predictions. Ultimately, this approach will serve as a general framework for the modelling of complex fluid-particle interactions in high shear reactors and mixing chambers with rotating flows.

CRediT authorship contribution statement

B. Oyegbile: Conceptualization, Methodology, Software, Visualization, Writing - original draft. **G. Akdogan:** Project administration, Writing - review & editing. **M. Karimi:** Software, Validation, Data curation.

Declaration of Competing Interest

The authors would like to notify that they have no affiliation with or involved in any organization or entity with financial interest or non-financial interest in the subject-matter or the content of this manuscript.

Acknowledgements

The authors gratefully acknowledge financial support from The World Academy of Sciences (TWAS) and National Research Foundation (NRF) for this study under the funding instrument number UID: 105553.

References

ANSYS Fluent Theory Guide 18.2, 2017.
ANSYS Fluent User's Guide 18.2, 2017.
Balachandar, S., Eaton, J.K., 2009. Turbulent Dispersed Multiphase Flow. Annu. Rev. Fluid Mech. 42, 111–133. https://doi.org/10.1146/annurev.fluid.010908.165243.
Bellani, G., Variano, E.A., 2012. Slip Velocity of Large Neutrally Buoyant Particles in Turbulent Flows. New J. Phys. 14.
Bodnár, T., Galdi, G.P., Nečasová, Š. (Eds.), 2017. Particles in Flows. Springer, Heidelberg.
Chaumeil, F., Crapper, M., 2014. Using the DEM-CFD Method to Predict Brownian

Particle Deposition in a Constricted Tube. Particuology 15, 94–106. https://doi.org/10.1016/j.partic.2013.05.005.
Childs, R.N.P., 2011. Rotating Flow. Elsevier, Oxford.
Chu, K.W., Yu, A.B., 2008. Numerical Simulation of Complex Particle–Fluid Flows. Powder Technol 179, 104–114. https://doi.org/10.1016/j.powtec.2007.06.017.
Cloete, S., Johansen, S.T., Amini, S., 2012. Performance Evaluation of a Complete Lagrangian KTGF Approach for Dilute Granular Flow Modelling. Powder Technol 226, 43–52. https://doi.org/10.1016/j.powtec.2012.04.010.
Darelius, A., Rasmuson, A., van Wachem, B., Niklasson Björn, I., Folestad, S., 2008. CFD Simulation of the High Shear Mixing Process Using Kinetic Theory of Granular Flow and Frictional Stress Models. Chem. Eng. Sci. 63, 2188–2197. https://doi.org/10.1016/j.ces.2008.01.018.
Derksen, J.J., 2003. Numerical Simulation of Solids Suspension in a Stirred Tank. AIChE J 49, 2700–2714. https://doi.org/10.1002/aic.690491104.
Fanelli, M., Feke, D.L., Manas-Zloczower, I., 2006. Modelling Dynamics of Dispersion of Nanoscale Particle Clusters. Plast. Rubber Compos. 35, 185–197. https://doi.org/10.1179/174328906X128207.
Furtney, J.K., Zhang, F., Han, Y., 2013. Review of Methods and Applications for Incorporating Fluid Flow in the Discrete Element Method. In: The Fifth International FLAC/DEM Symposium. Itasca International Inc., Hangzhou, China.
Gannt, J.A., Gatzke, E.P., 2006. Kinetic Theory of Granular Flow Limitations for Modeling High-Shear Mixing. Ind. Eng. Chem. Res. 45, 6721–6727. https://doi.org/10.1021/ie051267f.
Greifzu, F., Kratzsch, C., Forgber, T., Lindner, F., Schwarze, R., 2016. Assessment of Particle-Tracking Models for Dispersed Particle-Laden Flows Implemented in OpenFOAM and ANSYS FLUENT. Eng. Appl. Comput. Fluid Mech. 10, 30–43. https://doi.org/10.1080/19942060.2015.1104266.
Haghnegahdar, A., Feng, Y., Chen, X., Lin, J., 2018. Computational Analysis of Deposition and Translocation of Inhaled Nicotine and Acrolein in the Human Body with E-Cigarette Puffing Topographies. Aerosol Sci. Technol. 52, 483–493. https://doi.org/10.1080/02786826.2018.1447644.
Hashemisohi, A., Wang, L., Shahbazi, A., 2019. Dense Discrete Phase Model Coupled with Kinetic Theory of Granular Flow to Improve Predictions of Bubbling Fluidized Bed Hydrodynamics. KONA Powder Part. J. 36, 215–223. https://doi.org/10.14356/kona.2019017.
Hellesto, A., Ghaffari, M., Balakin, B., 2016. A Parametric Study of Cohesive Particle Agglomeration in a Shear Flow—Numerical Simulations by the Discrete Element Method. J. Dispers. Sci. Technol. 38, 611–620. https://doi.org/10.1080/01932691.2016.1185015.
Hobbs, A., 2004. Design and Optimization of a Vortex Particle Separator for a Hot Mix Asphalt Plant. In: International ANSYS Conference. ANSYS Inc., Pittsburgh, PA.
Li, Z., Derksen, J.J., Gao, Z., 2015. Models and Applications for Simulating Turbulent Solid–Liquid Suspensions in Stirred Tanks. J. Chem. Eng. Jpn. 48, 329–336. https://doi.org/10.1252/jcej.14we056.
Lukerchenko, N., Kvurt, Y., Keita, I., Chara, Z., Vlasak, P., 2012. Drag Force, Drag Torque, and Magnus Force Coefficients of Rotating Spherical Particle Moving in Fluid. Part. Sci. Technol. 30, 55–67. https://doi.org/10.1080/02726351.2010.544377.
Michaelides, E., Crowe, C.T., Schwarzkopf, J.D., 2016. Multiphase Flow Handbook, Second Edition. CRC Press, Boca Raton, FL.
Njobuenwu, D.O., Fairweather, M., 2018. Large Eddy Simulation of Particle Agglomeration with Shear Breakup in Turbulent Channel Flow. Phys. Fluids 30. https://doi.org/10.1063/1.5037174.
Norouzi, H.R., Zarghami, R., Sotudeh-Gharebagh, R., Mostoufi, N., 2016. Coupled CFD-DEM Modeling: Formulation, Implementation and Application to Multiphase Flows. John Wiley & Sons, Chichester.
Oyegbile, B., Akdogan, G., 2018. Hydrodynamic Characterization of Physicochemical Processes in Stirred Tanks and Agglomeration Reactors. In: Basha, O.M., Morsi, B.I. (Eds.), Chemical Engineering Laboratory Unit Operations and Experimental Methods. InTech, Rijeka, pp. 57–77.
Oyegbile, B., Akdogan, G., Karimi, M., 2018. Experimental and CFD Studies of the Hydrodynamics in Wet Agglomeration Process. ChemEngineering 2, 1–17. https://doi.org/10.3390/chemengineering2030032.
Oyegbile, Benjamin, Hoff, M., Adonadaga, M., Oyegbile, Brian, 2017. Experimental Analysis of the Hydrodynamics, Flow Pattern and Wet Agglomeration in Rotor-Stator Vortex Separators. J. Environ. Chem. Eng. 5, 2115–2127. https://doi.org/10.1016/j.jece.2017.04.016.
Passalacqua, A., Marmo, L., 2009. A Critical Comparison of Frictional Stress Models Applied to the Simulation of Bubbling Fluidized Beds. Chem. Eng. Sci. 64, 2795–2806. https://doi.org/10.1016/j.ces.2009.03.005.
Schellander, D., 2014. CFD Simulations of Particle Laden Flow: Particle Transport and Separation. Anchor Academic Publishing, Hamburg.
Taghizadeh, A., Hashemabadi, S.H., Yazdani, E., Akbari, S., 2018. Numerical Analysis of Restitution Coefficient, Rotational Speed and Particle Size Effects on the Hydrodynamics of Particles in a Rotating Drum. Granul. Matter 20, 1–13. https://doi.org/10.1007/s10035-018-0813-2.
Tu, J., Yeoh, G.-H., Liu, C., 2018. Computational Fluid Dynamics: A Practical Approach, 3rd ed. Butterworth-Heinemann, Oxford.
Vångö, M., Pirker, S., Lichtenegger, T., 2018. Unresolved CFD–DEM Modeling of Multiphase Flow in Densely Packed Particle Beds. Appl. Math. Model. 56, 501–516. https://doi.org/10.1016/j.apm.2017.12.008.
Wadnerka, D., Utika, R.P., Tade, M.O., Pareek, V.K., 2012. CFD Simulation of Solid–Liquid Stirred Tanks. Adv. Powder Technol. 23, 445–453. https://doi.org/10.1016/j.apt.2012.03.007.
Wadnerkar, D., Tade, M.O., Pareek, V.K., Utikar, R.P., 2016. CFD Simulation of Solid–Liquid Stirred Tanks for Low to Dense Solid Loading Systems. Particuology 29, 16–33. https://doi.org/10.1016/j.partic.2016.01.012.
Weber, M.W., Hrenya, C.M., 2006. Square-well Model for Cohesion in Fluidized Beds. Chem. Eng. Sci. 61, 4511–4527. https://doi.org/10.1016/j.ces.2006.02.008.
Xie, L., Luo, Z.-H., 2018. Modeling and Simulation of the Influences of Particle-Particle Interactions on Dense Solid–Liquid Suspensions in Stirred Vessels. Chem. Eng. Sci. 176, 439–453. https://doi.org/10.1016/j.ces.2017.11.017.
Yu, F., Xu, Z., Haghnegahdar, A., 2016. In: Volkov, K. (Ed.), Aerosols. InTech, Rijeka.
Zhu, H.P., Zhou, Z.Y., Yang, R.Y., Yu, A.B., 2007. Discrete Particle Simulation of Particulate Systems: Theoretical Developments. Chem. Eng. Sci. 62, 3378–3396. https://doi.org/10.1016/j.ces.2006.12.089.